DOI:10.28974/idojaras.2026.3.1

IDŐJÁRÁS

Quarterly Journal of the HungaroMet Hungarian Meteorological Service
Vol. 130, No. 3, July – September, 2026, pp. 225–243

Case studies of micro-meteorological wind simulations and turbulence analysis in Hong Kong during severe tropical storm Wutip in June 2025

Ka Wai Lo, **Kai Kwong Lai**, and **Pak Wai Chan***

Hong Kong Observatory,
134A Nathan Road, Kowloon, Hong Kong, China

**Corresponding author E-mail: pwchan@hko.gov.hk*

(Manuscript received in final form on January 8, 2026)

Abstract— Micrometeorological studies of a bridge and the urban area of Hong Kong under south to southwesterly winds associated with tropical cyclone Wutip in June 2025 were conducted using computational fluid dynamic simulation driven by a mesoscale model. For mean winds, such as 1-min or 10-min averages (as in the application to road traffic management on a bridge), the use of mesoscale meteorological models alone may be sufficient to capture the general wind trend, since the RMSEs of the mean wind speeds were comparable and mostly in the range of 1–5 m s^{-1}. However, if fluctuations in winds are considered and turbulence intensity is a concern for operation (such as the operation of drones in low-altitude economic activities), the coupling of mesoscale meteorological models with computational fluid dynamics models must be considered. However, the measured turbulence intensity could be rather high (40–50% for turbulence intensity), which may not be achieved with mesoscale coupled computational fluid dynamic models. Numerous issues remain to be resolved for this type of micro-meteorological studies, especially for studies and applications in urban meteorology. Future directions for these studies are also discussed.

Key-words: computational fluid dynamics (CFD), large eddy simulation (LES), turbulence intensity, tropical cyclone

1. Introduction

Microscale meteorological services that cover limited areas within a city have great application value. For instance, predicting wind speed trends and turbulence across sections of a long bridge is crucial for determining the cessation and resumption of road traffic (*Cai et al.*, 2015), particularly during tropical cyclones. Wind and turbulence measurements and forecasting in urban areas would be useful in several aspects, such as the comfort of pedestrians on the road (*Blocken* and *Carmeliet*, 2004) and the operation of drones for logistical purposes in low-altitude economy (LAE) (*Gianfelice et al.*, 2022).

Microclimatological monitoring (*Lefevre et al*., 2024; *Liu et al*., 2022; *Oke*, 2006), such as the setup of ultrasonic anemometers on bridges and lampposts (so-called smart lampposts) on roadsides, is becoming increasingly common. More experiments are being attempted to forecast microclimates, especially wind trends and turbulence metrics, such as turbulence intensity (the standard deviation of the wind speed divided by the mean wind speed).

Simulations of wind speed trends were previously performed by *Lo et al.* (2024a) for two tropical cyclones at a bridge in Hong Kong. A case study involving the simulation of an urban area in a tropical cyclone situation was also performed by *Lo et al.* (2024b). The present study is a continuation of the previous study, that focused on the severe tropical storm tip affecting Hong Kong from 14 to 15 June 2025. The Tseung Kwan O (TKO) bridge on the eastern side of the territory was considered. Simultaneously, a study was conducted for the downtown area of Hong Kong, namely, the Tsim Sha Tsui (TST) area. This study is novel in several ways.

1. In previous tropical cyclone studies, the winds were mainly northerlies. This study examined southerly winds induced by Wutip to assess the terrain and building impacts on microclimates across varying prevailing wind directions.
2. Following the previous study, *Lo et al.* (2024b), more microclimate stations were set up in the TST. Weather stations operate in various parts of the TST and their measurements are compared with a high-resolution numerical weather prediction (NWP) model coupled with a computational fluid dynamics (CFD) model.
3. Apart from the 1-min and 10-min mean winds in the previous studies, *Lo et al.* (2024a) and *Lo et al.* (2024b), the turbulence intensity was also considered. Unfortunately, the high-frequency wind data (e.g. per-second measurements) required to calculate the eddy dissipation rate (EDR) are unavailable from the TKO bridge and TST microclimate stations, precluding a direct comparison with sub-grid-scale EDR outputs from the NWP-CFD coupled model.

2. *Materials and methods*

2.1. Microclimate stations

A re-cap of the anemometer setup on the TKO bridge is shown in the upper panel of *Fig.1*. Eight anemometers were present in total. CB1 and CB2 were positioned at the bridge deck level. The other six anemometers were installed on two arc-shaped structures, with the highest points at CB5 and CB6, approximately 60 m above sea level.

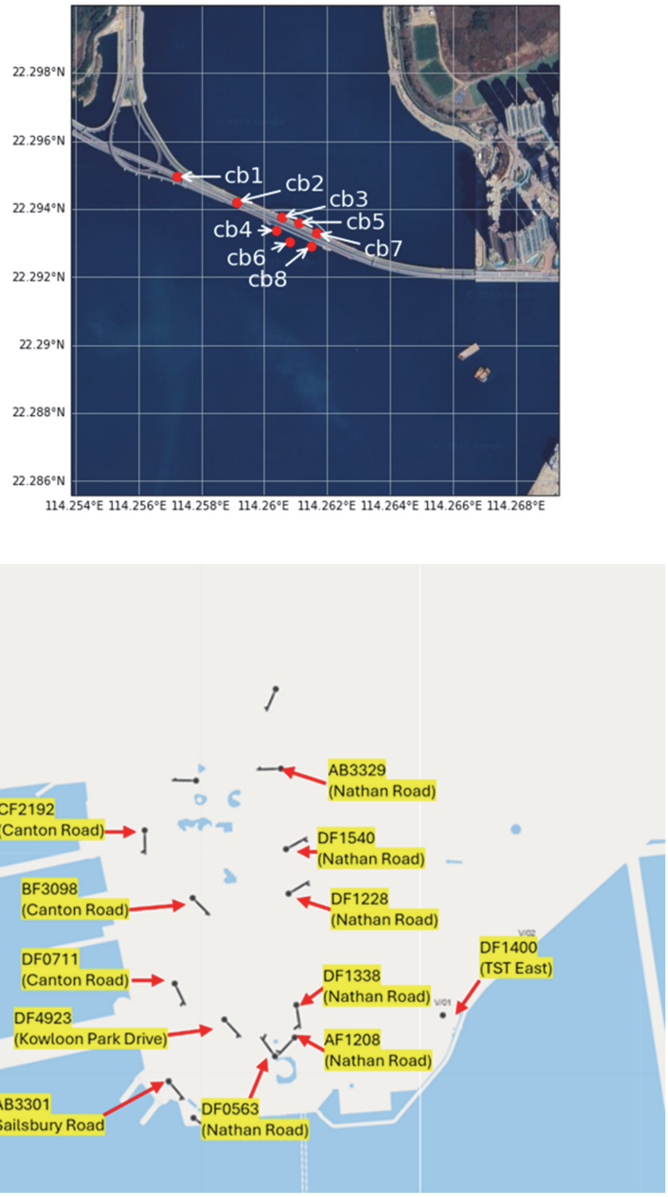

Fig.1. Location of the eight anemometers on the Tseung Kwan O bridge (upper panel) and location of the microclimate stations over the Tsim Sha Tsui area (lower panel).

The setup of the microclimate stations in the TST area is shown in the lower panel of *Fig.1*. Most of the stations were set up along the major roads in a general north-south orientation in the area, namely, Nathan Road and Canton Road. A couple of anemometers have better exposure to the seaside, namely, AB3301 near Star Pier and DF1400 on the coast of the TST East area.

2.2. Severe tropical storm Wutip

Surface isobaric charts for the mornings of June 14 and 15, 2025 are shown in the upper and lower panels of *Fig.2*, respectively. Wutip was initially located west of the Leizhou Peninsula in western Guangdong, China, over Beibu Wan. It then moved northeastward, crossing the southern part of China, and gradually weakened over land. The following morning, it was located approximately 300 km north of Hong Kong. Because of its circulation, southerly winds prevailed over Hong Kong on June 14, 2025. The wind direction gradually veered southwest. Under southerly wind situations, the TKO bridge and TST area are downstream of the mountains in Hong Kong. The terrain of the latter island may have induced turbulence in the two areas under investigation. Apart from the mean winds, the turbulence intensity was also studied in the present paper.

2.3. Numerical model setup

The mesoscale simulation employed the Regional Atmospheric Modelling System (RAMS v6.3) configured with six nested domains of progressively finer resolutions: 25 km, 5 km, 1 km, 200 m, 40 m, and 40 m. The fifth and sixth domains (both at 40 m resolution) were centered over the TKO and TST regions, respectively, to provide high-resolution wind fields for the targeted areas. These innermost domains also supplied the initial and boundary conditions for subsequent CFD simulations. The vertical grid started from a size of 75 m, with a stretching ratio of 1.08 applied to successive layers, and the maximum vertical spacing was capped at 2000 m. The turbulence closure for the innermost four domains utilized the Deardorff parameterization scheme (*Deardorff*, 1980).

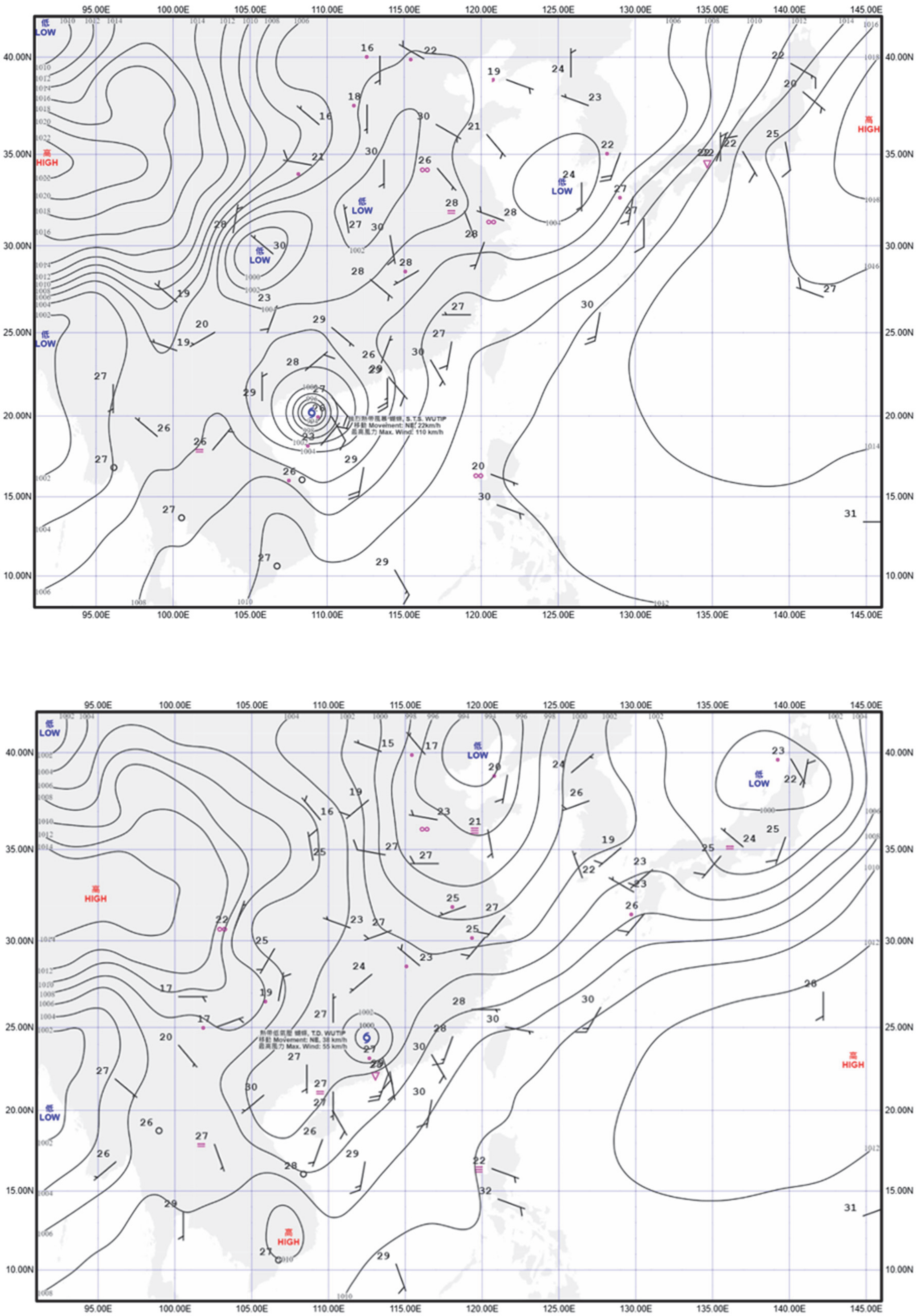

Fig.2. Surface isobaric charts at 8:00 a.m. on June 14, 2025 (upper panel) and at 8:00 a.m. on June 15, 2025 (lower panel). The local time has been followed (UTC+8).

Parallelized large-eddy simulation model PALM was used as the CFD software for this study (*Maronga et al.*, 2015, 2020; *Raasch* and *Schröter*, 2001). It is a parallelized large-eddy simulation (LES) model which solves filtered, nonhydrostatic, and incompressible Navier–Stokes equations under the Boussinesq approximation. PALM explicitly resolves energy-containing eddies while modeling subgrid-scale turbulence via a 1.5-order closure scheme based on the Deardorff parameterization (*Deardorff*, 1980). For the numerical schemes, a fifth-order upwind momentum advection scheme (*Wicker* and *Skamarock*, 2002) together with a third-order Runge-Kutta time-stepping method (*Williamson*, 1980) were used. The spatial resolution was set to 2 m horizontally, while vertically, a 2 m base grid was applied up to 50 m altitude, after which a stretching ratio of 1.08 was imposed, capping the maximum vertical grid spacing at 12 m. Synthetic turbulence was generated at the inflow boundaries (*Kim et al.*, 2013; *Xie* and *Castro*, 2008). The coupling between RAMS and PALM was performed using a dynamic file generated from the RAMS simulation data, which supplied the initial and boundary conditions required for the PALM simulation.

3. Results

3.1. Results for the TKO bridge

Numerical simulations generally capture trends in wind speed and wind direction changes at bridges. A snapshot of the wind distribution over the bridge is shown in the upper panel of *Fig.3*. The simulation was initialized at 12 UTC on June 14, 2025 and ran for 18 h till 06 UTC on June 15, 2025. A snapshot of the simulation results around the time of observation is shown in the lower panel of *Fig.3*. Strong south-to southwesterly winds (blue wind barbs in the lower panel of *Fig.3.*) prevailed in the bridge region. Gale force winds (red wind barbs) were simulated at isolated positions and were consistent with actual observations, particularly at the location of the two arc-shaped structures.

Fig.4. provides a general overview of the wind simulation results from the RAMS at a horizontal resolution of 40 m. The wind pattern at a height of approximately 60 m above the local terrain is shown in the upper panel of *Fig.4.* A gap prevails in the mountains of Hong Kong upstream of the island area. This gap flow results in a narrow south to southwesterly jet just over the bridge. Simultaneously, because of the terrain of Hong Kong Island, moderate to severe turbulence occurs downstream of such terrain (colored yellow to red in the lower panel of *Fig.4*, in the region of 0.3 to 0.5 $m^{2/3}s^{-1}$). This higher turbulence area only covers the sea channel and the TKO bridge is free of stronger turbulence.

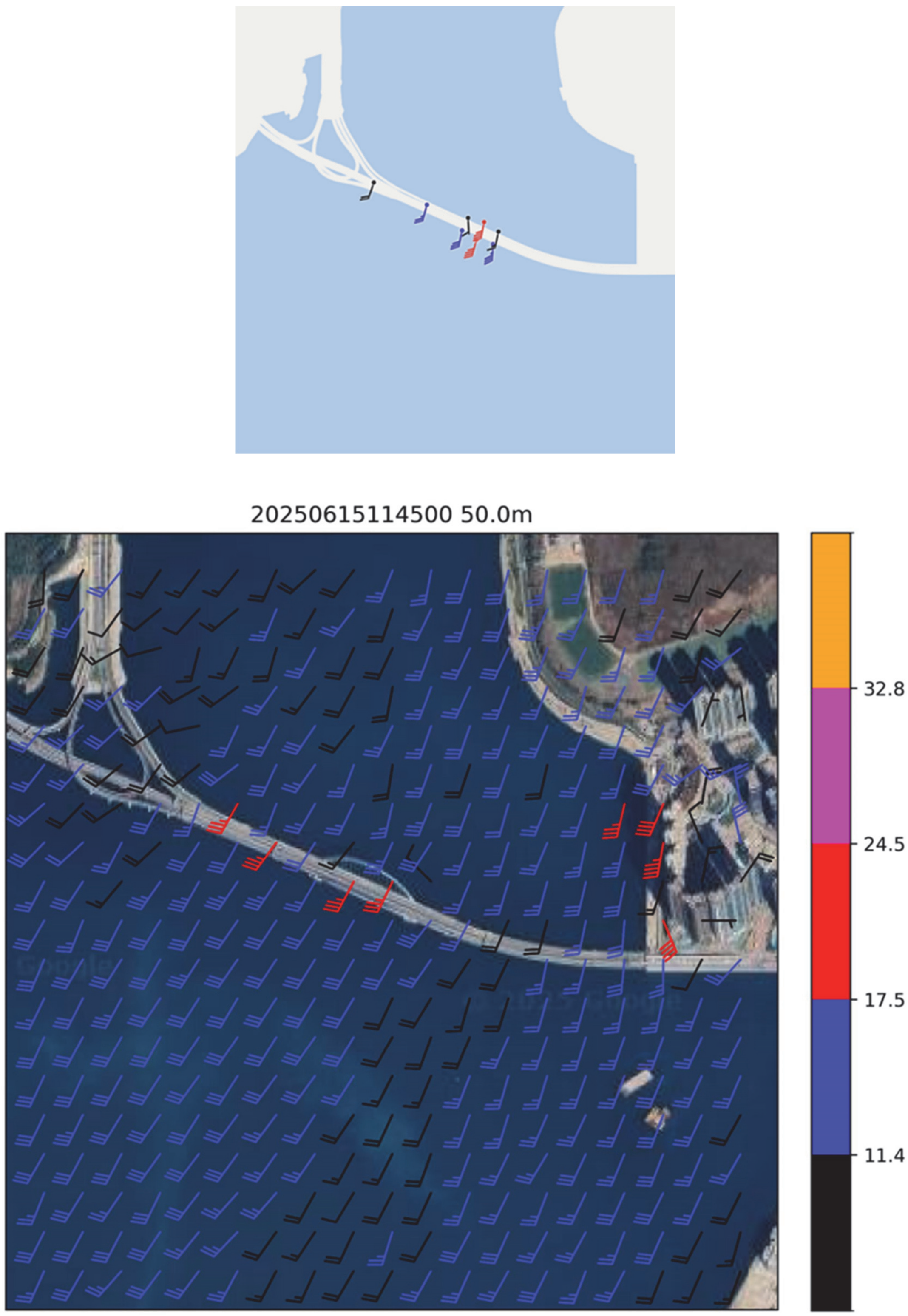

Fig. 3. Wind distributions over the TKO Bridge at 11:00 a.m. on June 15, 2025 (upper panel) and the simulated wind distribution by the PALM at 11:45 a.m. on the same day (lower panel). The local time has been followed (UTC+8).

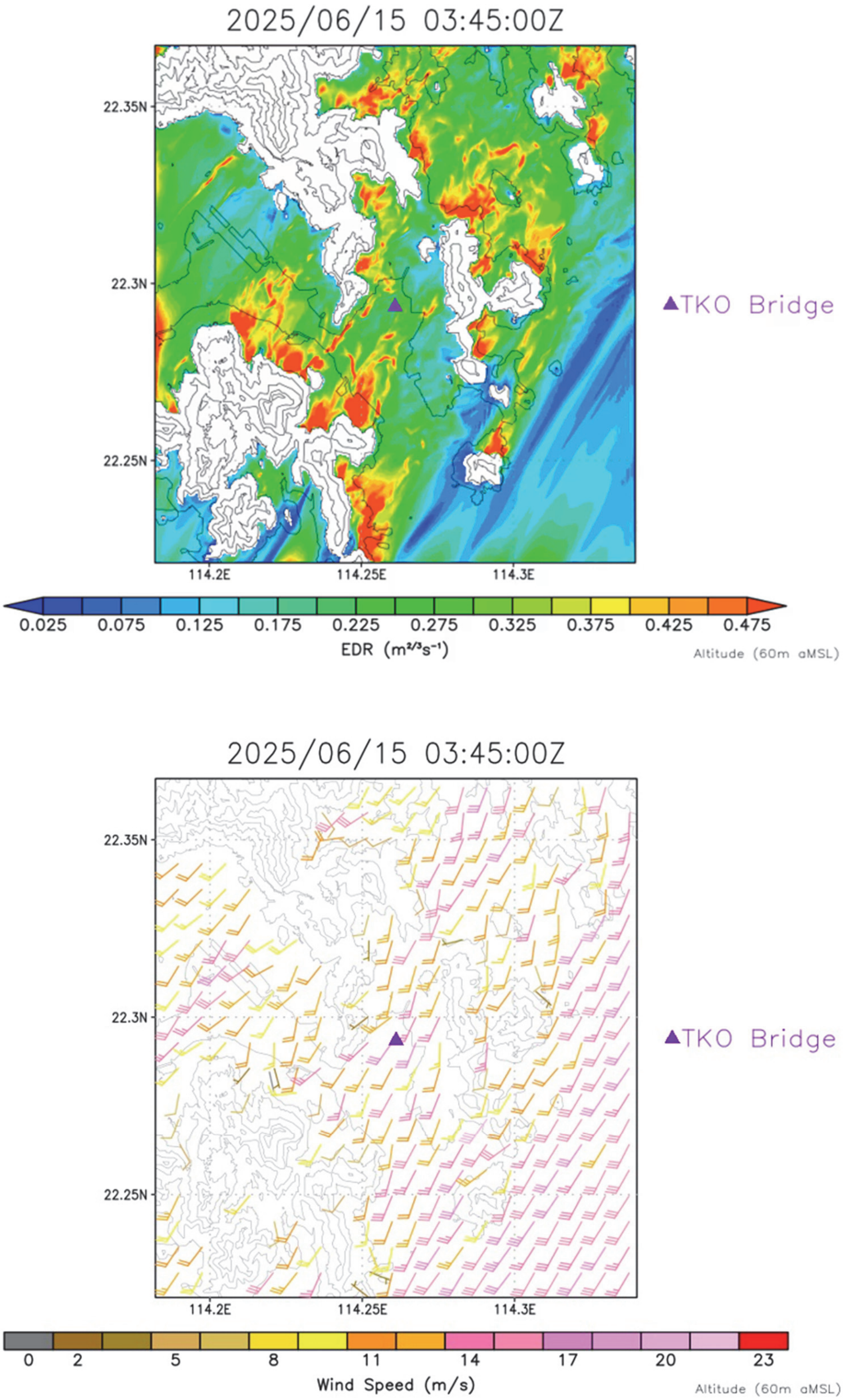

Fig.4. Winds (upper panel) and EDR (lower panel) simulation from RAMS at a height of around 60 m above local terrain at 11:45am on June 15, 2025, in local time.

The time series of the actual wind observations from the bridge are shown in *Fig.5*, where the upper panel shows the 1-min mean wind speed and the lower panel shows the 10-min mean wind direction. The simulation results were overlaid on them, with blue showing the RAMs results (at 40 m horizontal resolution) and red showing the PALM results. The following features were observed: (1) the wind speed and wind direction changes from the actual observations were generally well captured by both simulations for most anemometers, apart from isolated ones, such as CB3 and CB7; (2) the overall trend of RAMS and PALM simulation results were similar, and as such performing simulation at higher spatial resolution did not gain value in capturing finer changes in the time series of the observed wind speed and wind direction; (3) nonetheless, PALM results showed strong fluctuations, with magnitudes more comparable with the actual observations, as compared with the RAMS simulation results, and as such CFD simulation at higher spatial resolution had the value of providing more realistic fluctuations of the wind speed and wind direction, at least for 1-min averages.

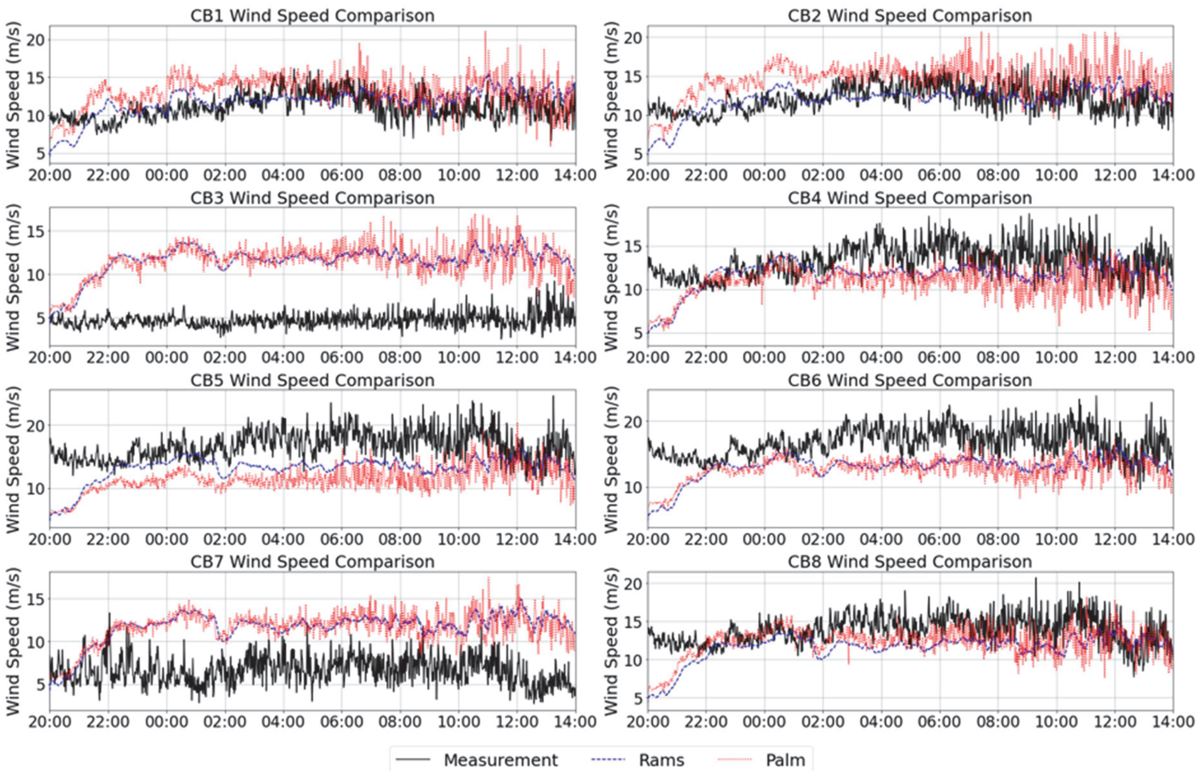

Fig. 5. Time series of the 1-min mean wind (upper panel) and 10-min wind direction (lower panel) at the eight anemometers on the TKO bridge from measurement, RAMS simulation, and PALM simulation.

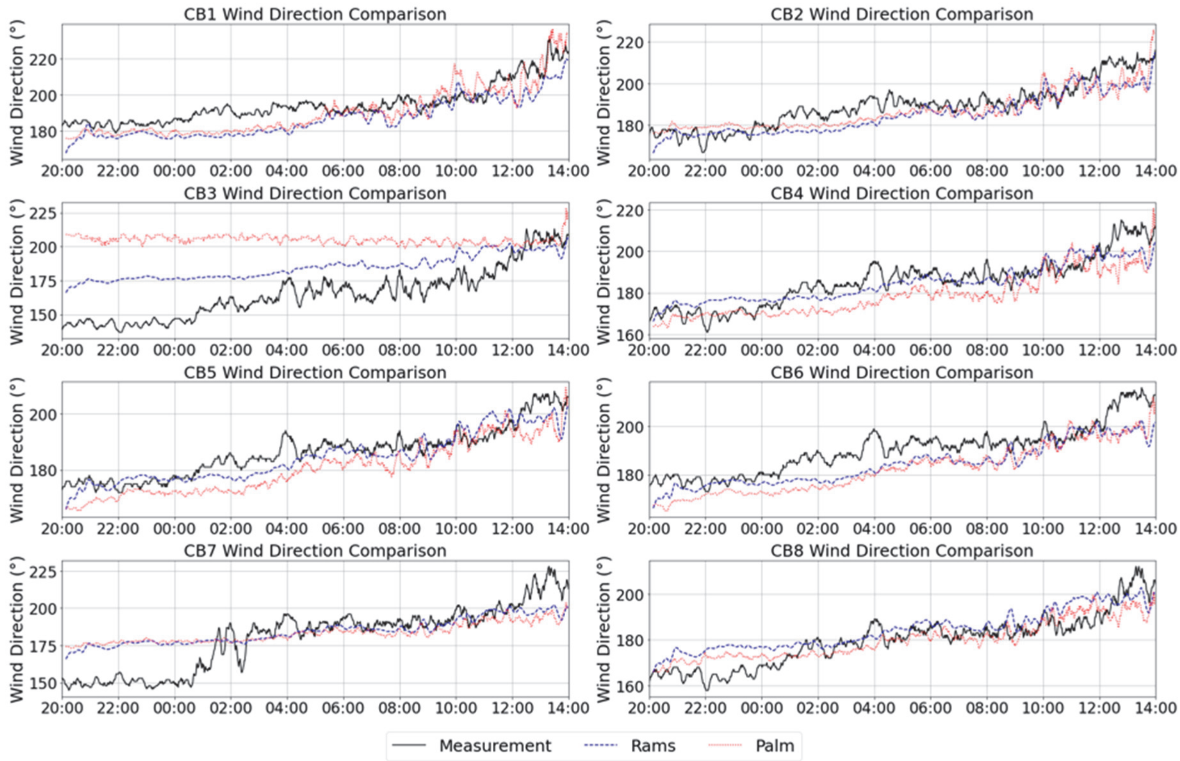

Fig.5. Continued

The quantitative comparison results are presented in *Table 1*. The period under consideration did not cover the first two hours of the simulation, allowing for spin-up of the models. The model simulations were compared directly with the anemometer measurements, and the root-mean-square errors (RMSEs) were calculated. From the perspective of RMSEs, the use of CFD simulation did not improve the forecasting results, namely, the RMSEs of RAMS alone and RAMS-CFD coupling were basically similar. However, as discussed above, RAMS-CFD captured the actual fluctuations in winds and had better application value.

Table 1. RMSE of wind speeds and direction from RAMS and PALM simulation compared to the measurement for eight anemometers over the TKO bridge

	CB1	**CB2**	**CB3**	**CB4**	**CB5**	**CB6**	**CB7**	**CB8**
RAMS Speed RMSE	2.04	1.85	7.42	2.45	4.04	4.08	5.86	2.80
PALM Speed RMSE	3.00	3.46	7.48	3.29	5.79	4.64	5.86	2.61
RAMS Direction RMSE	9.88	7.00	21.22	6.24	4.57	7.99	13.75	7.15
PALM Direction RMSE	8.12	6.33	41.45	9.61	7.16	9.24	15.09	6.06

As discussed previously, a new feature of the present study is the consideration of the turbulence intensity (TI). TI is calculated as the ratio of the standard deviation of wind speed to the mean wind speed over two-hour rolling window. The time series of the observed and simulated TIs is shown in *Fig. 6*. In general, from the actual observations, Tis showed an increasing trend with time.

Apart from the isolated anemometer (e.g. CB7), the trend was captured much better by the PALM simulation results than by RAMS alone. This is consistent with the previous observation that the RAMS-CFD coupled model captures the magnitude of the wind speed fluctuations, and this is reflected in forecasting the correct magnitude of the observed TIs.

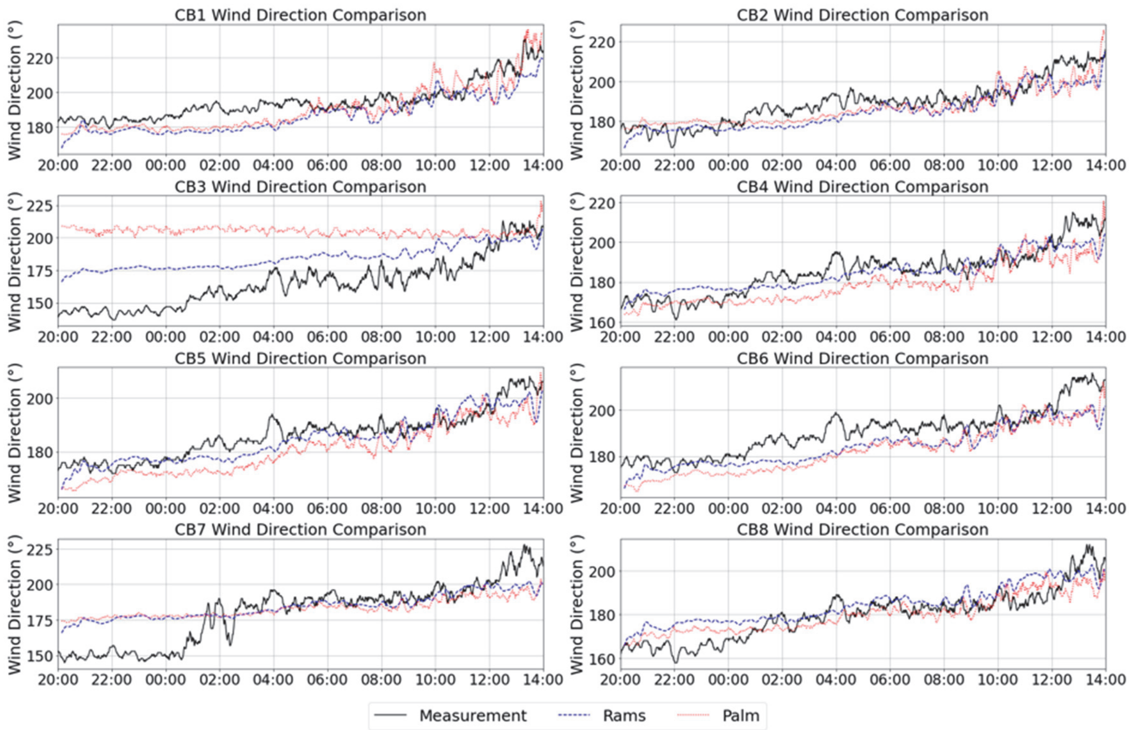

Fig. 6. Time series of turbulent intensity at the eight anemometers on the TKO bridge from measurement, RAMS simulation, and PALM simulation.

3.2. Results for the TST area

The study of the TST area is an urban meteorology issue; that is, with a highly developed area with several buildings, the value of the RAMS-CFD gain compared with the RAMS simulation alone (which considers the terrain and coastline only, without considering the buildings). A snapshot of the observations made by the microclimate station is shown in the upper panel of *Fig.7*. Two notable features exist, namely, southwestely flow at the southwestern corner of the TST area, which is more exposed in that direction toward the harbor, and a cyclonic feature observed at the southern part of Nathan Road, probably due to the interplay between terrain and buildings on the airflow. The corresponding simulation results are presented in the lower panel of *Fig.7*. This was a 15-h simulation as initialized at 12 UTC on June 14, 2025. Both features appeared well in the RAMS-CFD simulation results. In general, the available observations compared favorably with the simulation results, at least for this snapshot.

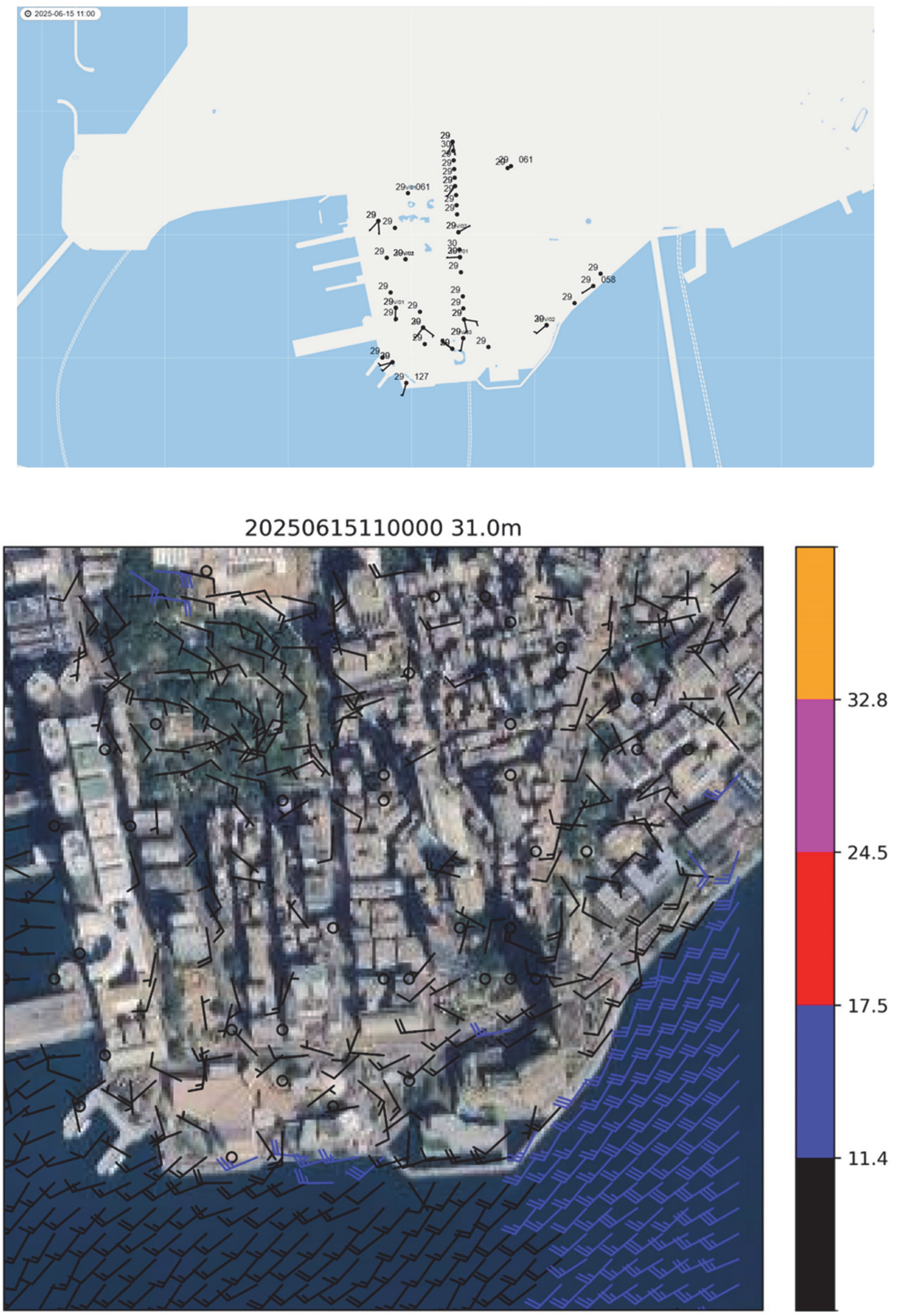

Figure 7 Wind measurement over the Tsim Sha Tsui area at 11:00 a.m. on June 15, 2025 (upper panel) and the simulated wind distribution by the PALM over the Tsim Sha Tsui area at the same time (lower panel). The local time has been followed (UTC+8).

As an indication of the flow pattern in the TST area owing to the terrain, the RAMS simulation results (for the innermost domain with a horizontal resolution of 40 m) are shown in *Fig.8*. The upper panels show the simulated wind near the surface. Owing to blockage by the terrain of Hong Kong Island, the TST area generally has lighter winds compared to, for instance, the more exposed sea area to the west in this southwesterly flow regime. Simultaneously, owing to the terrain effect, higher turbulence occurs in the TST area, as shown in the EDR distribution in the lower panel of *Fig.8*. However, no actual measurements exist to verify the EDR simulation results.

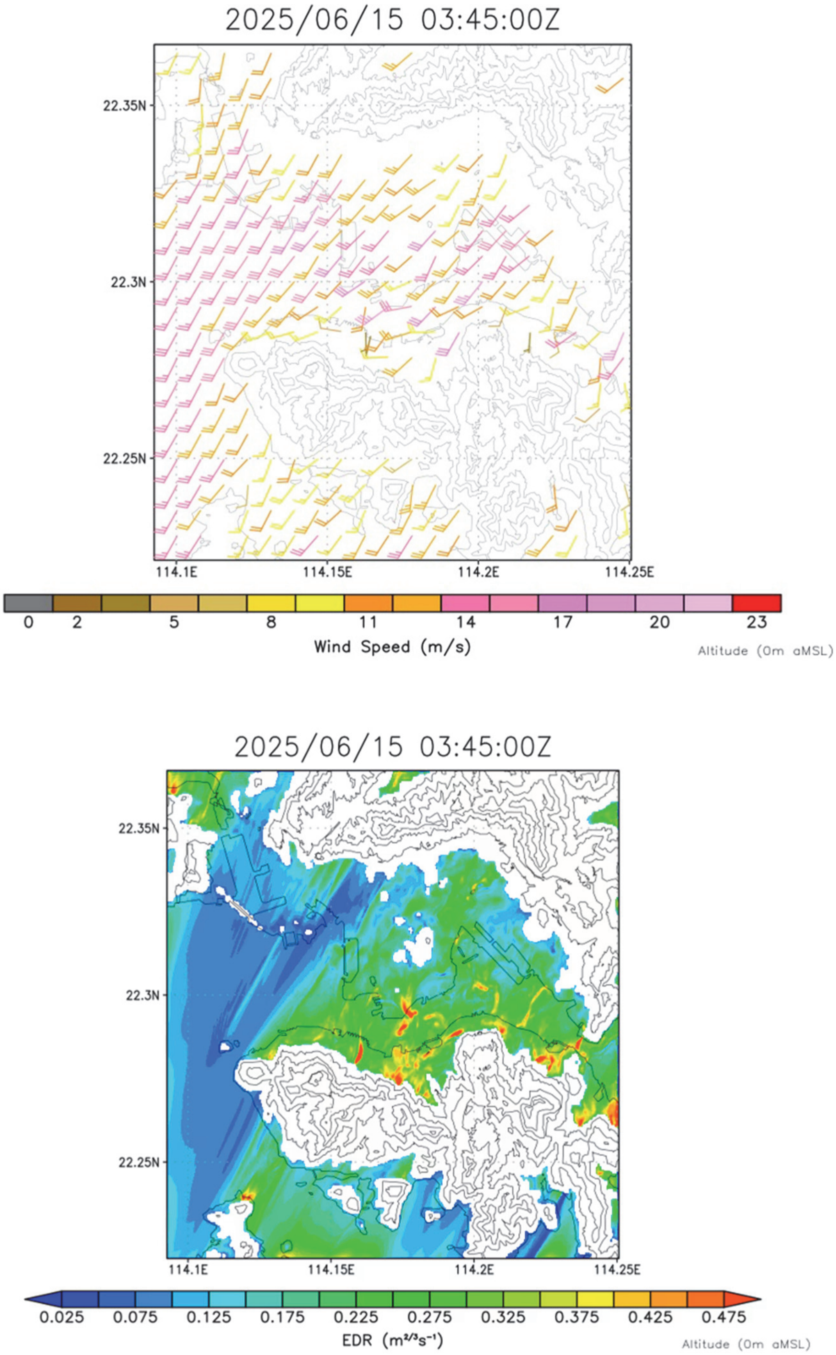

Fig. 8. Wind (upper panel) and EDR (lower panel) simulation from RAMS at 11:45 am on June 15, 2025, in local time

The time series of the observed and simulated (RAMS alone and RAMS-CFD) wind speeds and directions are shown in *Fig.9.* and *Fig.10.*, respectively. Several anemometers are present with blockage effect by the nearby buildings for this south to southwesterly flow regimes, e.g., DF1540, where the measured wind speed remains rather low compared to the RAMS simulation alone, which does not include building effect, and the measured wind direction deviates significantly from the ‘prevailing’ or ‘background’ wind direction of south to southwesterly. Similar features were also observed, for example for DF0563, which showed significant fluctuations in wind direction in the actual measurements.

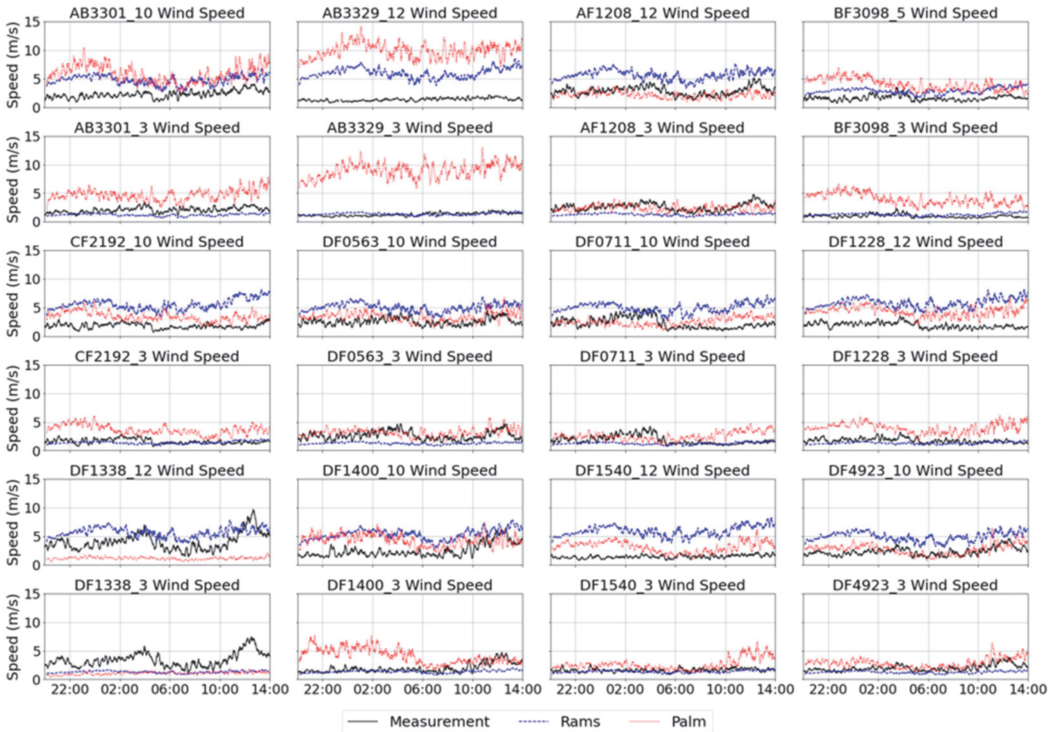

Fig. 9. Time series of the 10-min mean wind speed at the different microclimate stations over Tsim Sha Tsui from measurement, RAMS simulation, and PALM simulation.

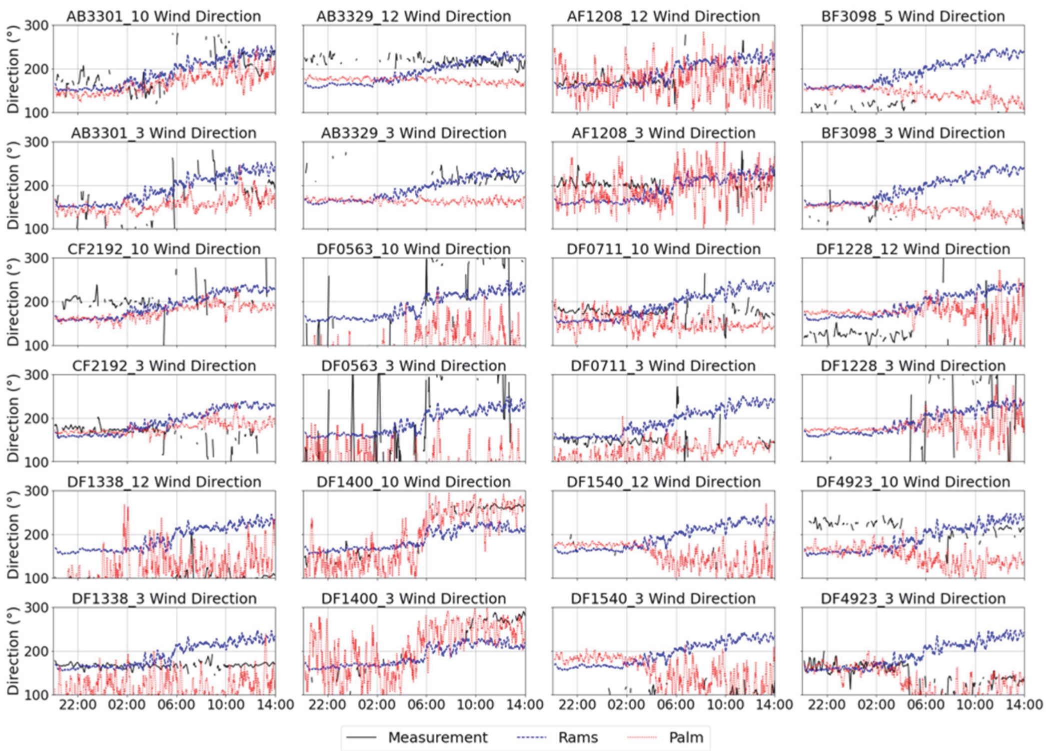

Fig.10. Time series of the 10-min mean wind direction at the different microclimate stations over Tsim Sha Tsui from measurement, RAMS simulation, and PALM simulation.

Moreover, from the perspective of RMSEs for mean winds (the mean 10-min averages are considered because they are used in the actual measurements), the addition of PALM in the simulation does not largely improve the accuracy when compared with the actual observations, as shown in Table 2. For both RAMS alone and RAMS-CFD, the RMSEs for wind speed and wind direction were similar. Sometimes, one set of results is better than the other for individual anemometers; however, in general, considering all stations, it may only be concluded that the RMSEs are comparable.

Table 2. RMSE of wind speeds and direction from RAMS and PALM simulation compared to the measurement for microclimate stations over TST

	AB3301_10	**AB3301_3**	**AB3329_12**	**AB3329_3**	**AF1208_12**	**AF1208_3**
RAMS Speed	2.81	0.97	5.23	0.40	3.54	1.30
PALM Speed	4.18	3.47	9.44	8.42	0.97	1.17
RAMS Direction	37.52	55.37	37.12	44.32	58.14	52.68
PALM Direction	49.93	63.77	46.92	64.91	65.38	57.02

	BF3098_3	**BF3098_5**	**CF2192_10**	**CF2192_3**	**DF0563_10**	**DF0563_3**
RAMS Speed	0.75	1.93	4.61	0.62	3.22	1.32
PALM Speed	2.79	2.25	1.91	2.55	2.05	1.71
RAMS Direction	126.94	136.42	80.68	100.55	99.12	113.57
PALM Direction	92.27	46.64	104.20	101.24	111.53	113.68

	DF0711_10	**DF0711_3**	**DF1228_12**	**DF1228_3**	**DF1338_12**	**DF1338_3**
RAMS Speed	3.90	0.91	4.98	0.58	2.50	2.32
PALM Speed	1.70	1.86	3.51	3.33	3.14	2.57
RAMS Direction	56.22	87.36	107.47	99.76	111.92	50.44
PALM Direction	39.27	57.82	111.19	121.08	60.56	49.71

	DF1400_10	**DF1400_3**	**DF1540_12**	**DF1540_3**	**DF4923_10**	**DF4923_3**
RAMS Speed	2.93	1.02	5.13	0.43	3.25	0.88
PALM Speed	2.08	2.26	1.77	1.65	1.14	1.63
RAMS Direction	44.37	58.32	73.88	116.93	50.30	94.34
PALM Direction	33.43	46.12	67.21	81.13	70.36	34.35

However, the inclusion of CFD has the advantage of capturing fluctuations in the wind, which is reflected in the comparison of the TI, as shown in *Fig.11*. Overall, the simulated TIs from RAMS-CFD compared much better with the actual measurements based on RAMS alone. The maximum achievable TIs from RAMS-CFD were generally higher. Notably, all anemometers show a peak TI in the middle part of the simulation, namely, around 06 Hong Kong time, on June 15, 2025 (which is around 22 UTC, June 14, 2025 with Hong Kong time = UTC + 8 h). This corresponds to the period when the wind direction is generally southerly; as such, significant blockage by the terrain of Hong Kong Island and disturbance of airflow by buildings, prevail. As a result, the terrain-induced turbulence was higher (higher value of standard deviation of the wind speed), and the wind speed just over the TST was rather low (lower value of mean wind speed), leading to a generally higher TI (expressed as the standard deviation of the wind divided by the 10-min mean wind speed). Even with the use of RAMS-PALM, the maximum TI could not be achieved (as high as 40–50%).

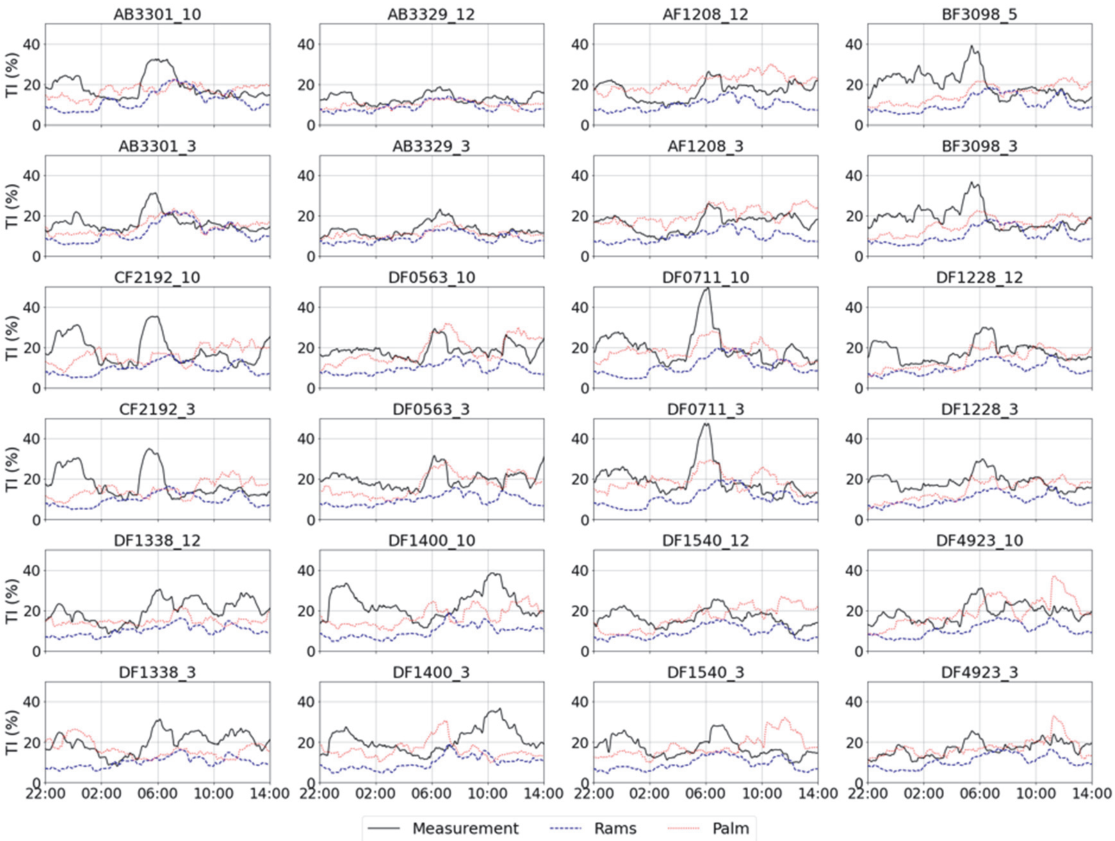

Fig. 11. Time series of turbulent intensity at the microclimate stations over Tsim Sha Tsui from measurement, RAMS simulation, and PALM simulation.

Further tuning and inclusion of more features in the simulation may be necessary to attain this extremely high level of TI. For example, refining the specification of surface roughness could be important, as turbulence can be sensitive to roughness (*Krogstadt*, 1999; *Kadivar*, 2021). Furthermore, the inclusion of trees in the model could be improve the simulation, as there are many trees along Nathan Road and Canton Road. Another aspect for further study is the consideration of EDR. The hardware and software of the smart lamppost microclimate stations would need to be modified to store second-level wind data so that the EDR can be calculated and compared with the sub-grid scale EDR from the model simulations.

4. Conclusions

This paper presents the RAMS and RAMS-CFD simulation results for a microclimate study in two regions in Hong Kong, namely, the TKO bridge (from a road traffic management perspective) and the TST area (from an urban meteorology perspective), during the strong south to southwesterly flow associated with a tropical cyclone (severe tropical storm Wutip) in June 2025. This study makes several notable observations. Firstly, although the inclusion of CFD did not improve the accuracy of the simulated mean winds (1-min or 10-min averages) based on RMSE statistics, the use of CFD helped capture the fluctuations in wind speed, as shown in the TI. Secondly, by comparing the measured data with the RAMS simulation alone and the RAMS-CFD simulation, the urban impact on the wind was clearly demonstrated, and the TIs simulated from RAMS-CFD generally had better results, although the maximum achievable TIs from actual observations remain unachieved. The results of this study suggest that, for mean wind speed in LAE applications, the use of mesoscale meteorological data alone may provide reasonable results. However, if turbulence needs to be considered, the inclusion of CFD is necessary, although sometimes the inclusion of CFD does not yet achieve the level of TI, as occasionally observed.

Turbulence is an interesting area with application value for future studies. The EDR is definitely an aspect that can be explored. If observations of EDR are available, then the impact of considering terrain alone (by mesoscale meteorological model) and both terrain and buildings (RAMS-CFD), which would provide a sufficiently accurate EDR for LAE application purposes, can be assessed. Secondly, upper-air wind measurements, for example, from ground-based Doppler LIDAR, remain unavailable. The inclusion of upper air wind data for comparison would yield more insight into the relative performance of RAMS alone and RAMS-CFD.

In addition, drone-based observations offer a promising pathway to address some of these observational gaps (*Hervo et al.*, 2023; *Inoue et al.*, 2025). Drones could provide targeted, high-resolution measurements of low-level wind profiles and turbulence-related quantities along critical corridors (e.g., bridge decks and urban street canyons), and could be used to derive turbulence metrics (including EDR proxies), where fixed stations are sparse. Such datasets would strengthen validation of both mean winds and turbulence characteristics, and could potentially support improved specification (or even assimilation) of boundary conditions for mesoscale-to-CFD coupling. These aspects — EDR observations, upper-air wind measurements, and the integration of drone-based measurements — will be the focus of our future studies.

References

Blocken, B. and *Carmeliet, J.,* 2004: Pedestrian Wind Environment around Buildings: Literature Review and Practical Examples. *Journal of Thermal Envelope and Building Science, 28(2),* 107–159. https://doi.org/10.1177/1097196304044396

Cai, C. S., Hu, J., Chen, S., Han, Y., Zhang, W., and *Kong, X.,* 2015: A coupled wind-vehicle-bridge system and its applications: a review. *Wind and Structures, 20(2),* 117–142. https://doi.org/10.12989/was.2015.20.2.117

Deardorff, J. W., 1980: Stratocumulus-capped mixed layers derived from a three-dimensional model. *Boundary-Layer Meteorology, 18(4),* 495–527. https://doi.org/10.1007/BF00119502

Gianfelice, M., Aboshosha, H., and Ghazal, T., 2022: Real-time Wind Predictions for Safe Drone Flights in Toronto. *Results in Engineering, 15, 100534.* https://doi.org/10.1016/j.rineng.2022.100534

Hervo, M., Romanens, G., Martucci, G., Weusthoff, T., and *Haefele, A.,* 2023: A. Evaluation of an Automatic Meteorological Drone Based on a 6-Month Measurement Campaign. *Atmosphere, 14, 1382.* https://doi.org/10.3390/atmos14091382

Inoue, J., Seko, H., Sato, K., and *Sakai, T.,* 2025: Operational capability of drone-based meteorological profiling in an urban area. *Journal of Geophysical Research: Atmospheres, 130, e2024JD041927.* https://doi.org/10.1029/2024JD041927

Kadivar, M., Tormey, D., and *McGranaghan, G.,* 2021: A review on turbulent flow over rough surfaces: Fundamentals and theories. *Int. J. Thermofluids 10, 100077.* https://doi.org/10.1016/j.ijft.2021.100077

Kim, Y., Castro, I. P., and *Xie, Z.-T.,* 2013: Divergence-free turbulence inflow conditions for large-eddy simulations with incompressible flow solvers. *Computers & Fluids, 84,* 56–68. https://doi.org/10.1016/j.compfluid.2013.06.001

Krogstadt, PÅ. and *Antonia, R.,* 1999: Surface roughness effects in turbulent boundary layers. *Experiments in Fluids 27,* 450–460. https://doi.org/10.1007/s003480050370

Lefevre, A., Malet-Damour, B., Boyer, H., and *Rivière, G.,* 2024: Advancing Urban Microclimate Monitoring: The Development of an Environmental Data Measurement Station Using a Low-Tech Approach. *Sustainability, 16(7), 3093.* https://doi.org/10.3390/su16073093

Liu, Z., Cheng, K. Y., He, Y., Jim, C. Y., Brown, R. D., Shi, Y., Lau, K., and *Ng, E.,* 2022: Microclimatic measurements in tropical cities: Systematic review and proposed guidelines. *Building and Environment, 222, 109411.* https://doi.org/10.1016/j.buildenv.2022.109411

Lo, K. W., Chan, P. W., Lai, K. K., Lau, S. P. W., and *Zhao, Z. H.,* 2024a: Case studies of the winds in the urban area of Hong Kong – Microclimate station observations and high resolution numerical simulations. *Heliyon, 10(18), e37865.* https://doi.org/10.1016/j.heliyon.2024.e37865

Lo, K.-W., Chan, P.-W., and *Lai, K.-K.,* 2024b: Observations and Simulations of the Winds at a Bridge in Hong Kong during Two Tropical Cyclone Events in 2023. *Applied Sciences, 14(17), 7789.* https://doi.org/10.3390/app14177789

Maronga, B., Banzhaf, S., Burmeister, C., Esch, T., Forkel, R., Fröhlich, D., Fuka, V., Gehrke, K. F., Geletič, J., Giersch, S., Gronemeier, T., Groß, G., Heldens, W., Hellsten, A., Hoffmann, F., Inagaki, A., Kadasch, E., Kanani-Sühring, F., Ketelsen, K., and *Raasch, S.,* 2020: Overview of the PALM model system 6.0. *In Geoscientific Model Development (Vol. 13, Issue 3).* https://doi.org/10.5194/gmd-13-1335-2020

Maronga, B., Gryschka, M., Heinze, R., Hoffmann, F., Kanani-Sühring, F., Keck, M., Ketelsen, K., Letzel, M. O., Sühring, M., and *Raasch, S.,* 2015: The Parallelized Large-Eddy Simulation Model (PALM) version 4.0 for atmospheric and oceanic flows: Model formulation, recent developments, and future perspectives. *Geoscientific Model Development, 8(8),* 2515–2551. https://doi.org/10.5194/gmd-8-2515-2015

Oke, T. R., 2006: Towards better scientific communication in urban climate. *Theoretical and Applied Climatology, 84(1–3),* 179–190. https://doi.org/10.1007/s00704-005-0153-0

Raasch, S. and *Schröter, M.,* 2001: PALM - A large-eddy simulation model performing on massively parallel computers. *Meteorologische Zeitschrift, 10(5),* 363–372. https://doi.org/10.1127/0941-2948/2001/0010-0363

Wicker, L. J. and *Skamarock, W. C.,* 2002: Time-Splitting Methods for Elastic Models Using Forward Time Schemes. *Monthly Weather Review, 130(8),* 2088–2097. https://doi.org/10.1175/1520-0493(2002)130<2088:TSMFEM>2.0.CO;2

Williamson, J. H., 1980: Low-storage Runge-Kutta schemes. *Journal of Computational Physics, 35(1),* 48–56. https://doi.org/10.1016/0021-9991(80)90033-9

Xie, Z.-T. and *Castro, I. P.,* 2008: Efficient Generation of Inflow Conditions for Large Eddy Simulation of Street-Scale Flows. *Flow, Turbulence and Combustion, 81(3),* 449–470. https://doi.org/10.1007/s10494-008-9151-5